
RIAV-MVS: Recurrent-Indexing an Asymmetric Volume for Multi-View Stereo

Changjiang Cai, Pan Ji*, Yi Xu

OPPO US Research Center

InnoPeak Technology, Inc., USA

{changjiang.cai,pan.ji,yi.xu}@innopeaktech.com

Abstract

In this paper, we present a learning-based approach for multi-view stereo (MVS), *i.e.*, estimate the depth map of a reference frame using posed multi-view images. Our core idea lies in leveraging a “learning-to-optimize” paradigm to iteratively index a plane-sweeping cost volume and regress the depth map via a convolutional Gated Recurrent Unit (GRU). Since the cost volume plays a paramount role in encoding the multi-view geometry, we aim to improve its construction both in pixel- and frame- levels. In the pixel level, we propose to break the symmetry of the Siamese network (which is typically used in MVS to extract image features) by introducing a transformer block to the reference image (but not to the source images). Such an asymmetric volume allows the network to extract global features from the reference image to predict its depth map. In view of the inaccuracy of poses between reference and source images, we propose to incorporate a residual pose network to make corrections to the relative poses, which essentially rectifies the cost volume in the frame-level. We conduct extensive experiments on real-world MVS datasets and show that our method achieves state-of-the-art performance in terms of both within-dataset evaluation and cross-dataset generalization.

1 Introduction

Multi-view stereo (MVS) aims to recover dense 3D geometry from multiple images captured from different viewpoints, with calibrated cameras [28]. It is a fundamental problem in computer vision and has wide applications ranging from autonomous driving [13, 57], remote sensing [3], augmented reality [52], to robotics [23]. Following a representative MVS method, *i.e.*, MVSNet [61], many learning based methods [18, 40, 41, 54, 55, 60, 62] have been proposed, achieving great improvements against their traditional counterparts [6, 15, 20, 46], in terms of the accuracy or efficiency.

Most of learning-based MVS methods [18, 40, 41, 54, 60, 62] rely on traditional plane-sweeping [15, 20] to generate a cost volume by comparing the CNN features of reference image and source images for matching at several depth hypotheses, and then apply 2D or 3D convolutional encoder-decoder architectures to aggregate and regularize the cost volume. Based on that, they will either apply 2D convolution (by reducing the depth channels via summation) to directly regress a depth map [18], or apply *soft-argmin* [32] to predict an expected depth from the distribution of the cost volume. The 2D CNN methods, use multi-level features as the skip connections to help decode the cost volume for depth regression. Even though the skip-connection from features improves the depth maps, they weaken the role of cost volume and the geometry knowledge embedded therein to some extent, and hence suffer from degraded generalization when testing on unseen domains. The 3D CNN methods use the *soft-argmin* to regress the depth map as the expectation from the cost volume distribution, and hence cannot handle well a flat or multi-modal distribution, *e.g.*, caused by textureless, repeated or

*Corresponding author

occluded regions, etc. Therefore, when this situation happens, the *soft-argmin* cannot well “classify” to target the best candidate, but instead gives an “average” prediction, by aggregating the undetected best candidate, the worst ones and the ones in the middle.

To mitigate those problems, we propose RIAV-MVS, a new paradigm to predict the depth via learning to recurrently index an asymmetric cost volume, obtaining improved accuracy and generalization. Our RIAV-MVS features several nontrivial novel designs.

First, we propose to predict the depth by learning to optimize the cost volume directly to iteratively estimate an *index field*. The proposed recurrent estimate of *index field* (a grid of indices to identify the depth hypotheses) enables the learning to be anchored at the cost volume domain. Specifically, it recurrently predicts the residual *index field*, so as to retrieve cost values for the next iteration, in a descent direction of matching cost, but also to directly index (*i.e.*, sampling via linear interpolation) depth hypotheses to render a depth map, which is iteratively optimized to approach the ground truth depth, making the system end-to-end trainable.

Second, to facilitate the optimization, we propose to improve the cost volume in pixel- and frame-levels, respectively. In the pixel level, a transformer block is asymmetrically applied to the reference view (but not to source views). This way, by capturing long-range global context via a transformer and pixel-wise local features via CNNs, we build an asymmetric cost volume to store more accurate matching similarity cues. In the frame level, we propose a residual pose net to rectify the camera poses, which are usually obtained via Visual SLAM [10, 17, 30] and inevitably contain noise, to more accurately backward warp the reference features to match its counterparts in source views.

We conduct extensive experiments on indoor-scene datasets, including ScanNet [16], 7-Scenes [21] and RGB-D Scenes V2 [33], and well-designed ablation studies to verify the effectiveness and the generalization of our approach.

2 Related Work

Depth can be accurately predicted from stereo matching, which can be broadly divided into binocular stereo and multi-view stereo (MVS). The former requires calibrated setups of rectified stereo pairs, and many traditional [4, 25, 26, 45] and deep learning based methods [8, 9, 11, 32, 34, 35, 42, 63, 64] have been proposed. Compared with binocular stereo, MVS methods estimate depth from a set of monocular images or a video, where the camera moves and the scene is assumed static. In this section, we briefly review deep learning based MVS methods.

3D-CNN MVS Depth Estimation. Learning-based MVS methods [18, 40, 41, 54, 55, 60–62] rely on traditional plane-sweeping [15, 20] to generate a cost volume by associating reference frame and source frames for similarity matching, followed by encoder-decoder architectures for cost volume aggregation and depth map prediction. Among them, MVSNet [61], R-MVSNet [62] and DPSNet [27], leverage 3D convolutions to regularize 4D cost volumes and regress depth maps via softargmin [32]. Different strategies have been introduced for cost volumes construction. MVSNet [61] proposes a variance-based cost volume for multi-view similarity measurement. Cas-MVSNet [22] builds cascade cost volumes based on multi-scale feature pyramid and regresses the depth map in a multi-stage coarse-to-fine manner. Similarly, Cheng *et al.* propose UCS-Net [14] to build cascade adaptive thin volumes by leveraging variance-based uncertainty. CVP-MVSNet [60] builds a cost volume pyramid via multi-scale images to reduce to memory footprint. This cost volume mechanism is also adopted to other related tasks, *e.g.*, 3D plane reconstruction in PlaneMVS [39], which proposes to leverage slanted plane sweeping to help plane reconstruction, achieving accurate depth predictions.

2D-CNN MVS Depth Estimation. Even though 3D convolutional methods usually deliver high accuracy, but they demand a large amount of memory footprint and computation cost. Instead, some methods, *e.g.*, MVDepthNet [56] and DeepVideoMVS [18], generate 3D volumes by computing correlation or dot production between the extracted features of multi-view input images. The 3D cost volumes are further regularized by 2D convolutions. DeepVideoMVS [18] extracts multi-scale features. It uses the feature at half scale to construct the cost volume, and other features as the skip connections to a series of decoders for depth regression. PatchmatchNet [55] proposes an adaptive procedure mimicking PatchMatch [6] to achieve superior efficiency. 2D convolutions are much faster and more memory efficient than the 3D counterparts, making them better suitable for lightweight networks in real-time applications.

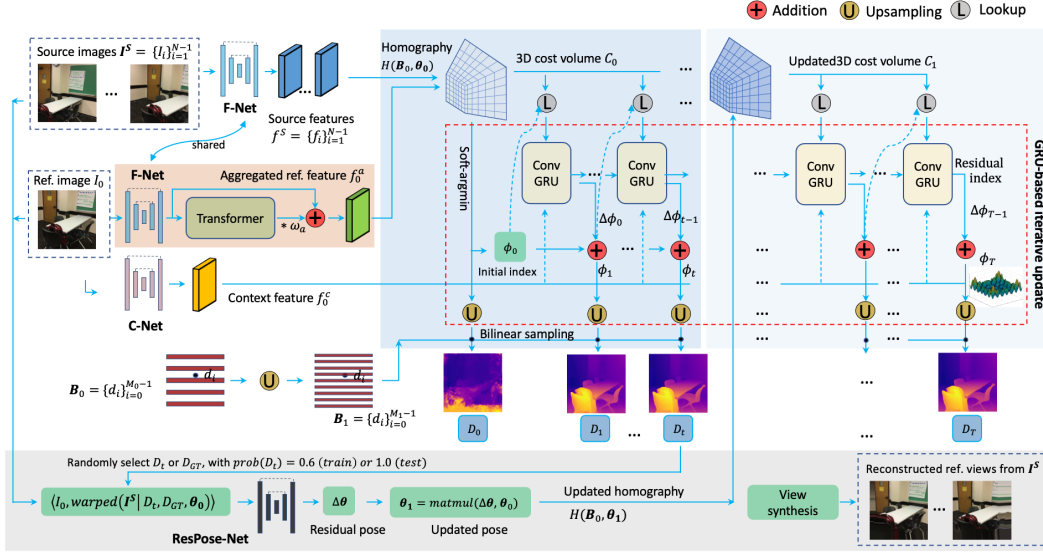


Figure 1: Architecture of our proposed network. It consists of a feature extraction (*i.e.*, F-Net, a Transformer, and C-Net) block, a cost volume construction and index field GRU-based optimization block, and a residual pose correction block.

Iterative Depth Estimation. A few methods have adopted an iterative depth estimation paradigm. R-MVSNet [62] iteratively regularizes each slice of the cost volume with GRU along the depth dimension. Unlike those cost volume based approaches before mentioned, Point-MVSNet [12] directly processes the target scene as point clouds. It first generates a coarse depth map, converts it into a point cloud and refines the point cloud iteratively to reduce the residual between the currently estimated depth and the ground truth depth. IterMVS [54] proposes to encode a pixel-wise probability distribution of depth in the hidden state of a GRU-based estimator. Each iteration, the multi-scale matching information is injected into the GRU to predict the depth and confidence maps to facilitate the following 3D reconstruction. The depth maps are predicted via a combined classification and regression through the probability distribution. It uses *arg-min* to finish the "classification" function, which is not differentiable and must be detached first before its following regression operation. Unlike IterMVS, our method learns to recurrently index the cost volume to directly find the best depth candidates in an end-to-end, differentiable way.

3 Method

Our learning-based end-to-end multi-view stereo system, RIAV-MVS, aims to predict depth maps from a set of images, different views of the same scene with known camera poses, denoted by $\mathcal{I} = \{I_i\}_{i=0}^{N-1}$. More specifically, it uses one as the reference image and others as source images to infer the depth map of the reference one. Without loss of generality, we refer to the first image I_0 as reference view and others as source views \mathcal{I}^S , with the superscript $(\cdot)^S$ for the set of source view indices $1, 2, \dots, N-1$. An overview of our approach is illustrated in Fig. 1. It consists of feature extraction (Sec. 3.1), cost volume construction via plane-sweeping stereo [15, 20] (Sec. 3.2), and cost volume optimization and depth prediction (Sec. 3.3). Details will be discussed as below.

3.1 Feature Extraction

Given a reference image I_0 and source images \mathcal{I}^S , we extract matching features for each of them by F-Net, and a context feature for I_0 by C-Net, as shown in Fig. 1.

Local Matching Feature Extraction. Our feature extractor F-Net is based on PairNet [18]. It is a lightweight Feature Pyramid Network (FPN) [36] on top of first fourteen layers of MnasNet [49]. Specifically, the reference input image $I_0 \in \mathbb{R}^{H \times W}$ is spatially scaled down until 1/32 scale, and recovered up to 1/2 scale, resulting in multi-scale features $\{f_{0,s} \in \mathbb{R}^{\frac{H}{s} \times \frac{W}{s} \times F_0}\}$ ($s=2,4,8,16$ and

$F_0=32$ for feature channels). Unlike the PairNet, where $f_{0,2}$ is used to construct the cost volume, and other features are used in the skip connections to a series of decoders for depth regression, we add an extra fusion layer \mathcal{G} to aggregate them into a matching feature f_0 at 1/4 scale, as

$$f_0 = \mathcal{G}(\langle f_{0,2} \downarrow_2, f_{0,4}, f_{0,8} \uparrow_2, f_{0,16} \uparrow_4 \rangle) \quad (1)$$

where the fusion layer \mathcal{G} is a sequence of operation of $\text{Conv}_{3 \times 3}$, batch normalization, ReLU, and $\text{Conv}_{1 \times 1}$, \downarrow_x and \uparrow_x for downsampling and upsampling by scale x , $\langle \cdot \rangle$ for concatenation along channel dimension, and $f_0 \in \mathbb{R}^{H/4 \times W/4 \times F_1}$ with $F_1=128$. Similarly, F-Net (with shared weights as that for I_0) is also applied to source views \mathcal{I}^S to extract a set of matching features $f^S = \{f_i \mid i \in \mathcal{S}\}$.

Global Matching Feature of Reference View. Besides the local, pixel-wise features extracted from CNNs, we also leverage global, long-range information to better guide the matching. Towards that, a transformer layer (four-head self-attention with positional encoding) [53] is applied to the local feature f_0 of the reference view, to construct an aggregated feature $f_0^a \in \mathbb{R}^{H/4 \times W/4 \times F_1}$ as

$$f_0^a = f_0 + \omega_\alpha \cdot \text{softmax} \left(\frac{(f_0 \cdot W^Q) \cdot (f_0 \cdot W^K)^T}{\sqrt{F_1}} (f_0 \cdot W^V) \right) \quad (2)$$

where ω_α is a learned scalar weight which is initialized to zero, and $W^Q, W^K \in \mathbb{R}^{F_1 \times hF_1}$, and $W^V \in \mathbb{R}^{F_1 \times F_1}$ are the projections matrices for query, key and value features, with $h=4$ for multi-head attention. The expression $A \cdot B$ means matrix multiplication of A and B . The final output f_0^a contains both the local and global information, which are balanced by the parameter ω_α , to enhance the following cost volume construction.

Please note that this transformer self-attention is only applied to the *reference view*, while the source views still possess the local features from CNNs. Our *asymmetric* employment of this transformer layer provides the capability to better balance the high-frequency features (by high-pass CNNs) and the low-frequency features by self-attention [43, 48]. The former is beneficial to image matching at local and structural regions, while the latter, with noisy information suppressed by the transformer’s spatial smoothing (serving as a low-pass filter), provides more global context cues for robust matching, especially for the areas full of low-texture, repeated patterns, and occlusion, etc. This way, our network can learn where to rely on global features over local features, and vice versa.

3.2 Cost Volume Construction

We use the global matching feature map f_0^a of I_0 and local matching features f^S of \mathcal{I}^S to build a cost volume. The cost (or matching) volume is defined on a 3D view frustum attached to the camera in perspective projection. It is generated by running the traditional plane-sweep stereo [15, 20] which uniformly samples $M_0=64$ plane hypotheses in the inverse depth space, s.t. $1/d \sim U(d_{\min}, d_{\max})$. Here d_{\min} and d_{\max} are the near and far planes of the 3D frustum, respectively. Following [18], we set $d_{\min}=0.25$ and $d_{\max}=20$ meters for indoor scenes, e.g., ScanNet [16].

For a given depth hypothesis d and known camera intrinsic matrices $\mathcal{K} = \{K_i\}_{i=0}^N$ and relative transformations $\Theta = \{R_{0,i} \mid t_{0,i}\}_{i=1}^N$ from reference view 0, to source views $i \in \mathcal{S}$, a cost map is computed by i) warping source view feature f_i into the reference view and ii) calculating the similarity between the reference global feature f_0^a and the warped feature \tilde{f}_i . To generate \tilde{f}_i , we implement the homography H as a backward 2D grid sampling. Specifically, a pixel $\mathbf{p} = (u, v, 1)^T$ in the reference view, will be warped to its counterpart $\tilde{\mathbf{p}}_i$ in source view i as follows:

$$\tilde{\mathbf{p}}_i = H(\mathbf{p} \mid d, \mathcal{K}, \Theta) = K_i \cdot (R_{0,i} \cdot (K_0^{-1} \cdot \mathbf{p} \cdot d) + t_{0,i}) \quad (3)$$

Then \tilde{f}_i is bilinearly sampled from f_i as $\tilde{f}_i(\mathbf{p}) = f_i(\tilde{\mathbf{p}}_i)$. Given the warped source view feature \tilde{f}_i and the reference feature f_0^a , the cost volume is formulated as $C_0(d) = \frac{1}{N-1} \sum_{i \in \mathcal{S}} \frac{f_0^a \cdot \tilde{f}_i^T}{\sqrt{F_1}}$. This way, we can construct a cost volume for all depth candidates $\mathcal{B}_0 = \{d_i\}_{i=0}^{M_0-1}$, resulting in a 3D tensor, denoted as $C_0 \in \mathbb{R}^{H/4 \times W/4 \times M_0}$.

3.3 GRU-based Iterative Optimization

We solve the depth prediction as learning to optimize the dense stereo matching problem [6, 25, 50, 59]. Given the generated cost volume C_0 as in Sec. 3.2, the depth estimation of the reference image, is formulated as finding the best solution $D^* = \operatorname{argmin}_D E(D, C_0)$, which minimizes an energy function $E(D, C_0)$ (including a data term and a smoothness term). Unfortunately, such a *global* minimization is NP-complete due to many discontinuity preserving energies [7], and approximate solutions are proposed by loosing the energy function, *e.g.*, the binocular stereo matching solved by Semi-Global Matching (SGM)[25]. In SGM, the matching cost C_0 is iteratively aggregated by summing the costs (of all 1D minimum cost paths that end in pixel \mathbf{p} at disparity d^2) when traversing from pixel $\mathbf{p} - \mathbf{r}$ to pixel \mathbf{p} in a direction \mathbf{r} (out of sixteen directions) and the best disparity at each pixel \mathbf{p} is given by $d^*(\mathbf{p}) = \operatorname{argmin}_d(C'(\mathbf{p}, d))$, with C' being the aggregated cost volume. Similar to SGM, we do not directly optimize the energy function E , but learn to process the cost volume C_0 .

However, several main problems still need to be solved. (1) SGM is not differentiable due to its winner-take-all (WTA) by argmin , making the system not being trained in an end-to-end manner. (2) Its differentiable counterpart, SGA [64], was proposed by changing the min to sum when aggregating the cost volume, and replacing the argmin with $\operatorname{softargmin}$ when predicting the disparity from the optimized cost volume, but still i) the update direction \mathbf{r} when traversing from pixel $\mathbf{p}-\mathbf{r}$ to \mathbf{p} needs to be predefined, and ii) the $\operatorname{softargmin}$ focusing on measuring the distance of the *expectation* of disparity map to the ground truth disparity, and hence cannot handle well multi-modal distributions in C_0 [54].

Therefore, towards an end-to-end, differentiable solution, we propose to use a GRU-based module to implicitly optimize the matching volume. It estimates a sequence of *index fields*, $\{\phi_t\}_{t=1}^T$ by unrolling the optimization problem to T iterative updates (in a descent direction), mimicking the updates of a first-order optimizer according to [1, 2, 37, 51]. At each iteration t , the index field $\phi_t \in \mathbb{R}^{H \times W}$ is estimated as a grid of indices to iteratively approach better (*i.e.*, closer to the ground truth) depth hypotheses having a lower matching cost. Specifically, a *residual* index field $\delta\phi_t$ is predicted as an update direction for next iteration, *i.e.*, $\phi_{t+1} = \phi_t + \delta\phi_t$, (analogous to the direction \mathbf{r} in SGM), which is explicitly driven by training the system (*e.g.*, feature encoders, the transformer layer, and the residual pose net, etc.) to minimize the loss between the predicted depth maps and the ground truth. The recurrent estimate of the index field enables the learning to be directly anchored at the cost volume domain. This indexing paradigm differentiates our approach from other depth estimation methods, such as the depth regression in 2D CNNs which fuses cost volume and the skipped multi-level features [18, 55, 54], and 3D CNNs by soft- argmin [32] after cost volume aggregation and regularization by 3D convolutions [22, 40, 61, 62].

Index Field Iterative Updates. We use a 3-level GRUs [37] to estimate a sequence of index fields, $\{\phi_t \in \mathbb{R}^{H/4 \times W/4}\}_{t=1}^T$ from an initial starting point ϕ_0 . We use a *softargmin-start* from the cost volume C_0 , *i.e.*, $\phi_0 = \sum_{i=0}^{M_1-1} i\sigma(C_0)$, where $\sigma(\cdot)$ is the softmax operator along the last dimension of cost volume C_0 , to convert it to a probability of each index i . This setup facilitates the convergence of our predictions. A four-layer matching pyramid $\{C_0^i \in \mathbb{R}^{H/4 \times W/4 \times M_0/2^i}\}_{i=1}^4$ is built by repeated pooling the cost volume C_0 along the depth dimension with kernel size 2 as in [51]. To index the matching pyramid, we define a lookup operator analogous to the one in [37]. Given a current estimate of index field ϕ_t , a 1D grid is constructed with integer offsets up to $r = \pm 4$ around the ϕ_t . The grid is used to index from each level of the matching pyramid via linear interpolation due to ϕ_t being real numbers. The retrieved cost values are then concatenated into a single feature map $C_0^{\phi_t} \in \mathbb{R}^{H/4 \times W/4 \times F_2}$. Then the index field ϕ_t , the retrieved cost features $C_0^{\phi_t}$, and context features f_0^c are concatenated, and fed into the GRU layer, together with a latent hidden state h_t . The GRU outputs a residual index field $\delta\phi_t$, and a new hidden state h_{t+1} :

$$\delta\phi_t, h_{t+1} \Leftarrow \operatorname{GRU}(\langle \phi_t, C_0^{\phi_t}, f_0^c \rangle, h_t), \text{ and } \phi_{t+1} \Leftarrow \phi_t + \delta\phi_t \quad (4)$$

Upsampling and Depth Estimation. The depth map at iteration t is estimated by sampling the depth hypotheses via linear interpolation given the index field ϕ_t . Since ϕ_t is at 1/4 resolution, we upsample it to full resolution using a convex combination of a 3×3 neighbors as in [51]. Specifically, a weight mask $W_0 \in \mathbb{R}^{H/4 \times W/4 \times (4 \times 4 \times 9)}$ is predicted from the hidden state h_t using two convolutional

²With an abuse of notation, d denotes both a depth value in MVS and a disparity value in binocular stereo.

layers and softmax is performed over the weights of those 9 neighbors. The final high resolution index field ϕ_t^u is obtained by taking a weighted combination over the 9 neighbors, and reshaping to the resolution $H \times W$. Convex combination can be implemented using the *einsum* function in PyTorch.

When constructing the cost volume, we use $M_0 = 64$ depth hypotheses, $\mathcal{B}_0 = \{d_i\}_{i=0}^{M_0-1}$. A small M_0 helps reduce the computation and space cost. If we use the upsampled index field ϕ_t^u to directly sample the planes \mathcal{B}_0 , we see *discontinuities* in the inferred depth map, even though the quantitative evaluation is not hindered. To mitigate it, we propose a coarse-to-fine pattern, and to use $M_1=256$ depth hypotheses $\mathcal{B}_1 = \{d_i\}_{i=0}^{M_1-1}$. Analogous to upsampling of optical flow or disparity in binocular stereo, the flow or disparity values themselves have to be scaled when implementing the spatial upsampling, our depth index fields are adjusted by a scale $s_D = \frac{M_1}{M_0} = 4$. To mimic the convex combination before mentioned, we apply a similar weighted summation along the depth dimension when sampling depth from \mathcal{B}_1 . Specifically, another mask $W_1 \in \mathbb{R}^{H \times W \times s_D \times M_0}$ is predicted from the hidden state using three convolutional layers, and further reshaped to $H \times W \times M_1$. Given a pixel \mathbf{p} , and the upsampled index field ϕ_t^u , the final depth D_t is estimated as

$$D_t(\mathbf{p}) = \frac{1}{\sum_{i=\phi_t^u(\mathbf{p})-r}^{\phi_t^u(\mathbf{p})+r} W_1(\mathbf{p}, [i])} \sum_{i=\phi_t^u(\mathbf{p})-r}^{\phi_t^u(\mathbf{p})+r} \mathcal{B}_1 [i] * W_1(\mathbf{p}, [i]) \quad (5)$$

where, we aggregate the neighbors within a radius $r = 4$ centered at the index $\phi_t^u(\mathbf{p})$ for a given pixel \mathbf{p} , and $[i]$ gives a greatest integer less than or equal to i , and $[i]$ means to index the depth planes \mathcal{B}_1 via linear interpolation, due to index i being a real number.

We would like to point out that our method embeds both regression (similar to *softargmin* in existing methods [40, 61, 62]) and classification (similar to *argmin*), which makes it robust to multi-modal distributions, and achieving *sub-pixel* precision due to linear interpolation. Combining both classification and regression has been seen in [54], but ours do not use the *argmax* operator when achieving the ‘‘classification’’ purpose, thanks to our proposal of estimates of index fields, which differentially bridges the cost volume indexing and depth hypotheses sampling directly in a sub-pixel precision.

Residual Pose Net. An accurate cost volume benefits the GRU-based iterative optimization. The quality of the generated cost volume C_0 is not only determined by the matching features (f_0^a and f^S) (for which we have proposed an asymmetric employment of the transformer layer), but also by the homography warping as in Eq. (3). But the camera poses are, in practice, usually obtained by Visual SLAM algorithms [10, 17, 30], and inevitably contains noise. Therefore, we propose a residual pose net to rectify the camera poses for accurately backward warping the reference features to match the corresponding features in source views. We use an image-net pretrained *ResNet18* [24] backbone as in [58, 29] to encode the reference image and the warped source images. Specifically, given the current estimated depth map D_t at iteration t , and the ground truth depth D_{gt} , we warp a source image I_i into the reference view through the homography defined in Eq. (3) with (noisy) ground truth camera poses Θ and the D_t or D_{gt} . We randomly select D_t or D_{gt} with a probability $\text{prob}(D_t)=0.6$ during network training, but always use the predicted depth D_t during network inference. The input to the pose net is the concatenated I_0 and the warped \tilde{I}_i , and the output is an axis-angle representation, which is further converted to a residual rotation matrix $\Delta\theta_i$, for an updated one $\theta'_i = \Delta\theta_i \cdot \theta_i$. This way, we predict the residual poses $\Delta\Theta = \{\Delta\theta_i\}_{i=1}^{N_v-1}$ for each of the source and reference pair, and do the rectification as $\Theta' = \Delta\Theta \cdot \Theta$. We leverage the updated poses Θ' to calculate a more accurate cost volume C_1 using Eq. (3), followed by the rest of iterations of GRU.

3.4 Loss Function

Our network is supervised on the inverse l_1 loss between the predicted depths $\{D_t\}_{i=1}^T$ and the ground truth D_{gt} . The loss is evaluated over the valid pixels which have ground truth depths. Following the exponentially increasing weights as in [37, 51], the loss is defined as

$$\mathcal{L} = \sum_{t=1}^T \gamma^{T-t} \frac{1}{N_v} \sum_{i=0}^{N_v-1} \left\| \frac{1}{D_t(i)} - \frac{1}{D_{gt}(i)} \right\|_1 \quad (6)$$

where, $\|\cdot\|_1$ measures the l_1 distance, N_v is the number of valid pixels, and $\gamma = 0.9$ in our experiments. We additionally apply the photometric loss (as defined in [58]) to supervise the residual pose network.

4 Experiments

4.1 Datasets

Our experiments use three indoor-scene datasets, which have RGB-D video frames with ground truth depths and known camera poses. ScanNet [16] is used in training and testing, and 7scenes [21] and RGB-D Scenes V2 [33] are evaluated for zero-shot generalization. (1) **ScanNet**. Our network is trained from scratch on ScanNet [16] using the official training split. Following the frame selection heuristic in [18], considering appropriate view frustum overlap and sufficient baselines, we sample 279,494 training samples and 20,000 validation ones. Each sample contains 3 frames, with one as reference frame and the others as source frames. For testing, we use ScanNet’s official test split (with 100 sequences from scene707 to scene806) and sample every 10 frames following [40], resulting in 20,668 samples for quantitative evaluation. Each sample contains N frames, with the middle one as reference, and the surroundings as source frames. Here we set $N=3$ or 5 , and compare the performances with different number of views. We set the valid depth range as $d_{min}=0.25$ and $d_{max}=20$ meters, for networking training and metric calculation. ScanNet has images in 640×480 resolution. In training, they are resized to 256×256 with cropping following [18]. For inference, the input images are resized to 320×256 without cropping. The predicted depth maps are upsampled with nearest neighbor interpolation to the original resolution 640×480 before calculating the quantitative metrics. (2) **7-Scenes**. We select 13 sequences from 7-Scenes for zero-shot generalization. The valid depth range is set the same as that on ScanNet. We generate a test set with 1,610 samples (each with 5 frames, at 640×480 resolution) by sampling the sequences every 10 frames. (3) **RGB-D Scenes V2**. It contains indoor scenes, including chair, sofa, table, bowls, caps, cereal boxes, coffee mugs, and soda cans, etc. We select 8 sequences for testing. Similarly, we sample the video sequence every 10 frames to generate 610 testing samples (each with 5 frames). See more details about train/val/test splits in the supplement.

4.2 Experimental Setup

Implementation Details. Our model is implemented in PyTorch [44], and trained end-to-end with a mini-batch size of 8 per NVIDIA RTX A6000 GPU. During training, we use the AdamW optimizer and clip gradients to the range $[-1, 1]$. When generating the cost volume by plane-sweep stereo, we set the plane hypotheses number as $M_0=64$; while predicting the final depth using index field, we set the plane hypotheses number as $M_1=256$. The same hyperparameters as in [37] are adopted for the context network and 3-level GRU architecture.

Training Schedule. Our network is trained for 20 epochs, with an initial learning rate of $1e-4$ and decayed by half at epoch 4^{th} and 8^{th} , respectively. For fair comparison, we also train the baselines PairNet [18] and IterMVS [54] on the same training samples of ScanNet for 20 epochs, using the official codes. For the baseline PairNet we follow the suggested learning rate scheduler, and for the baseline Iter-MVS, we use a learning rate of $1e-4$, which is decayed by half at epoch 4^{th} and 8^{th} .

4.3 Comparison with Existing Methods

In this section, we evaluate our method and compare it with several state-of-the-art deep-learning based MVS methods. Our network is strictly compared with two baselines PairNet [18] and IterMVS [54], following the same training schedule and training set. We also compare our method with other MVS methods either by running the provided models or referring the available evaluation metrics when testing on the same datasets, including ESTDepth [40], Neural RGBD [38], MVDepthNet [56], DPSNet[27], and DELTAS [47].

Quantitative Evaluation. We evaluate the depth maps using the standard metrics in [19], including mean absolute relative error (abs-rel), mean absolute error (abs), squared relative error (sq-rel), root mean square error in linear scale (rmse) and log scale (rmse-log), and inlier ratios under thresholds of $\sigma < 1.25/1.25^2/1.25^3$. Tab. 1 shows the results on the ScanNet benchmark of our methods and several state-of-the-art MVS methods. We compare three variants of our models: i) *base*: a base version

Method	ScanNet Test-Set							
	abs-rel	abs	sq-rel	rmse	rmse-log	$\delta < 1.25$	$\delta < 1.25^2$	$\delta < 1.25^3$
MVDepth [56]	0.1167	0.2301	0.0596	0.3236	0.1610	0.8453	0.9639	0.9906
MVDepth-FT	0.1116	0.2087	0.0763	0.3143	0.1500	0.8804	0.9734	0.9919
DPSNet [27]	0.1200	0.2104	0.0688	0.3139	0.1604	0.8640	0.9612	0.9860
DPSNet-FT	0.0986	0.1998	0.0459	0.2840	0.1348	0.8880	0.9785	0.9920
DELTA [47]	0.0915	0.1710	0.0327	0.2390	0.1226	0.9147	0.9872	0.9970
NRGBD [38]	0.1013	0.1657	0.0502	0.2500	0.1315	0.9160	0.9790	0.9927
ESTD [40]	<u>0.0812</u>	<u>0.1505</u>	<u>0.0298</u>	<u>0.2199</u>	<u>0.1104</u>	0.9313	0.9871	0.9968
PairNet [18]	0.0895	0.1709	0.0615	0.2734	0.1208	0.9172	0.9804	0.9928
IterMVS [54]	0.0991	0.1818	0.0518	0.2733	0.1368	0.8995	0.9741	0.9915
Ours(base)	0.0885	0.1605	0.0380	0.2347	0.1183	0.9211	0.9810	0.9939
Ours(+pose)	0.0827	0.1523	0.0343	0.2253	0.1131	0.9277	0.9830	0.9947
Ours(+pose,atten)	0.0747	0.1392	0.0288	0.2080	0.1038	0.9382	0.9858	0.9960

Table 1: Quantitative evaluation results on the test set of ScanNet [16]. Error metrics (lower is better) are abs-rel, abs, sq-rel, rmse, rmse-log, while accuracy (higher is better) metrics are $\delta < 1.25/1.25^2/1.25^3$. Here *-FT* denotes finetuned on ScanNet. *Bold* is the best score, and *underline* indicates the second best one.

ScanNet \Rightarrow Others	7-Scenes					RGB-D Scenes V2				
	abs-rel	abs	sq-rel	rmse	$\delta < 1.25$	abs-rel	abs	sq-rel	rmse	$\delta < 1.25$
NRGBD [38]	0.2334	0.4060	0.2163	0.5358	0.6803	-	-	-	-	-
ESTD [40]	0.1465	0.2528	0.0729	0.3382	0.8036	-	-	-	-	-
PairNet [18]	0.1157	0.2086	0.0677	0.2926	0.8768	0.0995	0.1382	0.0279	0.1971	0.9393
IterMVS [54]	0.1336	0.2363	0.1033	0.3425	0.8518	0.0811	0.1245	0.0340	0.2133	0.9496
Ours(base)	0.1148	0.1999	0.0552	0.2857	0.8726	0.0967	0.1336	0.0246	0.1836	0.9427
Ours(+pose)	0.1096	0.1930	0.0531	0.2775	0.8840	0.0812	0.1155	0.0193	0.1661	0.9627
Ours(+pose,atten)	0.1000	0.1781	0.0473	0.2664	0.8967	0.0803	0.1168	0.0200	0.1703	0.9632

Table 2: Zero-shot generalization from ScanNet [16] to 7-scenes [21] and RGB-D Scenes V2 [33]. Our methods achieve better generalization. We sample the sequences every 10 frames, and each sample has 5 frames for multi-view stereo depth prediction.

with our recurrent indexing cost volume, ii) *+pose*: with residual pose net, and iii) *+pose,atten*: a full version with residual pose and the asymmetric employment of transformer self-attention. Our full model achieves the best performance in most metrics except two inlier ratios under $\sigma < 1.25^2$ and 1.25^3 , outperformed by DELTAS [47] and ESTD [40]. But these two inlier ratios are quite loose metrics, not as essential as abs-rel and abs.

Zero-shot Generalization. We evaluate the generalization performance of our method RIAV-MVS from ScanNet to other indoor datasets without any fine-tuning. Tab. 2 shows the results, given the methods trained on ScanNet [16] and directly tested on 7-scenes [21] and RGB-D Scenes V2 [33]. Our models outperforms the baselines, and our three variants all have strong generalization performance.

Qualitative Results. Fig. 2 demonstrates the qualitative results of our method vs baselines IterMVS [54] and PairNet [18] on the test set of ScanNet. Our method can make more accurate and sharp depth prediction, especially for regions near boundary and edges. For both the near and far objects, our method outperforms the baselines.

4.4 Ablation Study

Iter. T	abs-rel	abs	$\delta < 1.25$	View No.	abs-rel	abs	$\delta < 1.25$	Sampling	abs-rel	abs	$\delta < 1.25$
16	0.1413	0.0760	0.9364	3 (base)	0.1204	0.2121	0.8603	s10 (base)	0.0885	0.1605	0.9211
24	0.1400	0.0752	0.9375	5 (base)	0.1148	0.1999	0.8726	key (base)	0.0838	0.1598	0.9277
48	0.1392	0.0747	0.9382	3 (+pose)	0.1162	0.2061	0.8711	s10 (+pose)	0.0827	0.1523	0.9277
64	0.1392	0.0746	0.9384	5 (+pose)	0.1096	0.1930	0.8840	key (+pose)	0.0789	0.1531	0.9339
96	0.1392	0.0745	0.9385	3 (+pose,atten)	0.1084	0.1923	0.8833	s10 (+pose,atten)	0.0747	0.1392	0.9382
128	0.1394	0.0745	0.9385	5 (+pose,atten)	0.1000	0.1781	0.8967	key (+pose,atten)	0.0697	0.1348	0.9472

(a) GRU iterations number on ScanNet test set

(b) View numbers, with ScanNet to 7-Scenes.

(c) View selection on ScanNet test set

Table 3: Ablation study of design choices. *Bold* is the best, and *underline* indicates the second best.

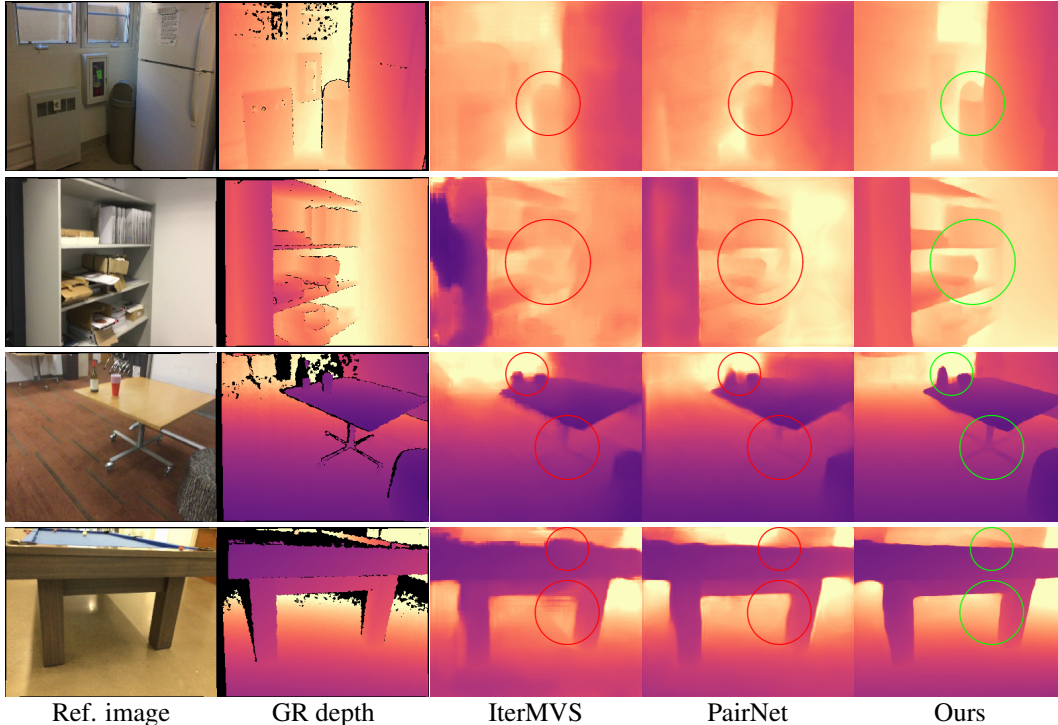


Figure 2: Qualitative results on ScanNet [16] test set. Left two columns show reference image and ground truth depth, and other columns are the estimated depth by baseline IterMVS [54], PairNet [18] and ours (the full version), respectively. Our method outperform the baselines on thin structures, small objects and boundaries, as highlighted in green for ours and in red for the baselines.

Efficacy of Proposed Modules. We have verified our design by ablating the modules to three variants, as shown in Tab. 1 and Tab. 2. The *base* version itself can achieve competitive performance on ScanNet and better generalization, verifying the efficacy of our novel design - cost volume recurrent indexing via index field. Further, the performance can be consistently boosted when the residual pose net (i.e., variant *+pose*) and transformer self-attention are added (i.e., variant *+pose,atten*). Therefore, each of the proposed modules can consistently help with accurate depth estimation.

Number of GRU Iterations and Convergence. Tab. 3-(a) shows the ablation study on different number of GRU iterations T . The results are obtained by running our model (the full version) on the ScanNet test set, with $T = 16, 24, 48, 64, 96$ and 128. Running more iterations boosts our depth prediction, but after $T \geq 96$, the gain becomes marginal.

View Number. We compare 3 views (1 as reference and 2 as source frames) and 5 views (1 as reference and 4 as source frames). Tab. 3-(b) shows, the more frames are used for matching, the better the depth will be. The results are for the zero-shot generalization from ScanNet to 7-Scenes. Please note that our full version model (*+pose,atten*) with 3-view input, outperforms the other two variants with 5-view input, showing the asymmetrical employment of the transformer self-attention can boost the prediction due to the mining of more global information.

Frame Sampling. We compare the simple view selection strategy (i.e., sampling by every 10 frames), with the heuristic way introduced in [18]. Tab. 3-(c) shows our methods can be further improved when the selected views have more overlapping and the baselines between them are suitable. Our(*+pose,atten*) even with simple strategy outperforms other variants with heuristic sampling, and so are our(*+pose*) vs our(*base*), verifying the effectiveness of each module.

5 Conclusions

We have proposed RIAV-MVS, a novel learning-based MVS method. Our approach exploits a convolutional GRU to iteratively optimize the index fields of the cost volume for depth regression.

The cost volume construction is further improved via the incorporation of a transformer block to the reference image and a residual pose network to correct the relative poses. The extensive experiments on ScanNet [16], 7-Scenes [21] and RGB-D Scenes V2 [33] have demonstrated the superior accuracy and cross-dataset generalization capability of our method.

Due to the plane sweeping cost volume construction and transformer self-attention, our method requires high memory consumption for high-resolution images and the inference time is not as fast as the light-weight, convolutional counterparts due to the iterative update paradigm in ours. For the future work, we would like to exploit the temporal information to further improve the depth estimation from posed-video streams.

References

- [1] J. Adler and O. Öktem. Solving ill-posed inverse problems using iterative deep neural networks. *Inverse Problems*, 33(12):124007, 2017.
- [2] J. Adler and O. Öktem. Learned primal-dual reconstruction. *IEEE transactions on medical imaging*, 37(6):1322–1332, 2018.
- [3] S. Agarwal, Y. Furukawa, N. Snavely, I. Simon, B. Curless, S. M. Seitz, and R. Szeliski. Building rome in a day. *Communications of the ACM*, 54(10):105–112, 2011.
- [4] K. Batsos, C. Cai, and P. Mordohai. CBMV: A coalesced bidirectional matching volume for disparity estimation. In *CVPR*, pages 2060–2069, 2018.
- [5] S. F. Bhat, I. Alhashim, and P. Wonka. AdaBins: Depth estimation using adaptive bins. In *CVPR*, pages 4009–4018, 2021.
- [6] M. Bleyer, C. Rhemann, and C. Rother. PatchMatch Stereo - stereo matching with slanted support windows. In *BMVC*, volume 11, pages 1–11, 2011.
- [7] Y. Boykov, O. Veksler, and R. Zabih. Fast approximate energy minimization via graph cuts. *PAMI*, 23(11):1222–1239, 2001.
- [8] C. Cai and P. Mordohai. Do end-to-end stereo algorithms under-utilize information? In *3DV*, pages 374–383, 2020.
- [9] C. Cai, M. Poggi, S. Mattoccia, and P. Mordohai. Matching-space stereo networks for cross-domain generalization. In *3DV*, pages 364–373, 2020.
- [10] C. Campos, R. Elvira, J. J. G. Rodríguez, J. M. Montiel, and J. D. Tardós. Orb-slam3: An accurate open-source library for visual, visual-inertial, and multimap slam. *IEEE Transactions on Robotics*, 37(6):1874–1890, 2021.
- [11] J.-R. Chang and Y.-S. Chen. Pyramid stereo matching network. In *CVPR*, pages 5410–5418, 2018.
- [12] R. Chen, S. Han, J. Xu, and H. Su. Point-based multi-view stereo network. In *ICCV*, pages 1538–1547, 2019.
- [13] X. Chen, H. Ma, J. Wan, B. Li, and T. Xia. Multi-view 3d object detection network for autonomous driving. In *CVPR*, July 2017.
- [14] S. Cheng, Z. Xu, S. Zhu, Z. Li, L. E. Li, R. Ramamoorthi, and H. Su. Deep stereo using adaptive thin volume representation with uncertainty awareness. In *CVPR*, 2020.
- [15] R. T. Collins. A space-sweep approach to true multi-image matching. In *CVPR*, 1996.
- [16] A. Dai, A. X. Chang, M. Savva, M. Halber, T. Funkhouser, and M. Nießner. Scannet: Richly-annotated 3d reconstructions of indoor scenes. In *CVPR*, 2017.
- [17] A. Dai, M. Nießner, M. Zollhöfer, S. Izadi, and C. Theobalt. Bundlefusion: Real-time globally consistent 3d reconstruction using on-the-fly surface reintegration. *ToG*, 36(4):1, 2017.
- [18] A. Düzçeker, S. Galliani, C. Vogel, P. Speciale, M. Dusmanu, and M. Pollefeys. DeepVideoMVS: Multi-view stereo on video with recurrent spatio-temporal fusion. In *CVPR*, 2021.
- [19] D. Eigen, C. Puhrsch, and R. Fergus. Depth map prediction from a single image using a multi-scale deep network. In *NeurIPS*, volume 27, 2014.
- [20] D. Gallup, J.-M. Frahm, P. Mordohai, Q. Yang, and M. Pollefeys. Real-time plane-sweeping stereo with multiple sweeping directions. In *CVPR*, pages 1–8, 2007.
- [21] B. Glocker, S. Izadi, J. Shotton, and A. Criminisi. Real-time rgb-d camera relocalization. In *International Symposium on Mixed and Augmented Reality (ISMAR)*. IEEE, October 2013.
- [22] X. Gu, Z. Fan, S. Zhu, Z. Dai, F. Tan, and P. Tan. Cascade cost volume for high-resolution multi-view stereo and stereo matching. In *CVPR*, 2020.
- [23] C. Häne, C. Zach, J. Lim, A. Ranganathan, and M. Pollefeys. Stereo depth map fusion for robot navigation. In *IROS*, pages 1618–1625. IEEE, 2011.
- [24] K. He, X. Zhang, S. Ren, and J. Sun. Deep residual learning for image recognition. In *CVPR*, pages 770–778, 2016.
- [25] H. Hirschmüller. Stereo processing by semiglobal matching and mutual information. *PAMI*, 30(2):328–341, 2008.
- [26] X. Hu and P. Mordohai. A quantitative evaluation of confidence measures for stereo vision. *PAMI*, 34(11):2121–2133, 2012.
- [27] S. Im, H.-G. Jeon, S. Lin, and I. S. Kweon. Dpsnet: end-to-end deep plane sweep stereo. In *ICLR*, 2019.
- [28] M. Ji, J. Gall, H. Zheng, Y. Liu, and L. Fang. SurfaceNet: An end-to-end 3d neural network for multiview stereopsis. In *ICCV*, pages 2307–2315, 2017.

- [29] P. Ji, R. Li, B. Bhanu, and Y. Xu. Monoindoor: Towards good practice of self-supervised monocular depth estimation for indoor environments. In *ICCV*, pages 12787–12796, 2021.
- [30] P. Ji, Q. Yan, Y. Ma, and Y. Xu. Georefine: Self-supervised online depth refinement for accurate dense mapping. *arXiv preprint arXiv:2205.01656*, 2022.
- [31] S. Jiang, D. Campbell, Y. Lu, H. Li, and R. Hartley. Learning to estimate hidden motions with global motion aggregation. In *ICCV*, pages 9772–9781, 2021.
- [32] A. Kendall, H. Martirosyan, S. Dasgupta, P. Henry, R. Kennedy, A. Bachrach, and A. Bry. End-to-end learning of geometry and context for deep stereo regression. In *ICCV*, pages 66–75, 2017.
- [33] K. Lai, L. Bo, and D. Fox. Unsupervised feature learning for 3d scene labeling. In *ICRA*, pages 3050–3057. IEEE, 2014.
- [34] J. Li, P. Wang, P. Xiong, T. Cai, Z. Yan, L. Yang, J. Liu, H. Fan, and S. Liu. Practical stereo matching via cascaded recurrent network with adaptive correlation. In *CVPR*, 2022.
- [35] Z. Liang, Y. Feng, Y. Guo, H. Liu, W. Chen, L. Qiao, L. Zhou, and J. Zhang. Learning for disparity estimation through feature constancy. In *CVPR*, pages 2811–2820, 2018.
- [36] T. Lin, P. Dollar, R. Girshick, K. He, B. Hariharan, and S. Belongie. Feature pyramid networks for object detection. In *CVPR*, pages 936–944, jul 2017.
- [37] L. Lipson, Z. Teed, and J. Deng. Raft-Stereo: Multilevel recurrent field transforms for stereo matching. In *3DV*, pages 218–227. IEEE, 2021.
- [38] C. Liu, J. Gu, K. Kim, S. G. Narasimhan, and J. Kautz. Neural RGB->D Sensing: Depth and uncertainty from a video camera. In *CVPR*, pages 10986–10995, 2019.
- [39] J. Liu, P. Ji, N. Bansal, C. Cai, Q. Yan, X. Huang, and Y. Xu. PlaneMVS: 3d plane reconstruction from multi-view stereo. In *CVPR*, 2022.
- [40] X. Long, L. Liu, W. Li, C. Theobalt, and W. Wang. Multi-view depth estimation using epipolar spatio-temporal networks. In *CVPR*, pages 8258–8267, June 2021.
- [41] K. Luo, T. Guan, L. Ju, H. Huang, and Y. Luo. P-mvsnet: Learning patch-wise matching confidence aggregation for multi-view stereo. In *ICCV*, pages 10452–10461, 2019.
- [42] N. Mayer, E. Ilg, P. Hausser, P. Fischer, D. Cremers, A. Dosovitskiy, and T. Brox. A large dataset to train convolutional networks for disparity, optical flow, and scene flow estimation. In *CVPR*, pages 4040–4048, 2016.
- [43] N. Park and S. Kim. How do vision transformers work? In *ICLR*, 2022.
- [44] A. Paszke, S. Gross, F. Massa, A. Lerer, J. Bradbury, G. Chanan, T. Killeen, Z. Lin, N. Gimelshein, L. Antiga, A. Desmaison, A. Kopf, E. Yang, Z. DeVito, M. Raison, A. Tejani, S. Chilamkurthy, B. Steiner, L. Fang, J. Bai, and S. Chintala. Pytorch: An imperative style, high-performance deep learning library. In *NeurIPS*, pages 8024–8035, 2019.
- [45] D. Scharstein and R. Szeliski. A taxonomy and evaluation of dense two-frame stereo correspondence algorithms. *IJCV*, 47(1-3):7–42, 2002.
- [46] J. L. Schönberger and J.-M. Frahm. Structure-from-Motion Revisited. In *CVPR*, 2016.
- [47] A. Sinha, Z. Murez, J. Bartolozzi, V. Badrinarayanan, and A. Rabinovich. DELTAS: Depth estimation by learning triangulation and densification of sparse points. In *ECCV*, pages 104–121, 2020.
- [48] X. Sui, S. Li, X. Geng, Y. Wu, X. Xu, Y. Liu, R. S. M. Goh, and H. Zhu. Craft: Cross-attentional flow transformers for robust optical flow. In *CVPR*, 2022.
- [49] M. Tan, B. Chen, R. Pang, V. Vasudevan, M. Sandler, A. Howard, and Q. V. Le. MnasNet: Platform-aware neural architecture search for mobile. In *CVPR*, pages 2820–2828, 2019.
- [50] T. Tani, Y. Matsushita, Y. Sato, and T. Naemura. Continuous 3D label stereo matching using local expansion moves. *PAMI*, 40(11):2725–2739, 2018.
- [51] Z. Teed and J. Deng. RAFT: Recurrent all-pairs field transforms for optical flow. In *ECCV*, pages 402–419. Springer, 2020.
- [52] J. Valentin, A. Kowdle, J. T. Barron, N. Wadhwa, M. Dzitsiuk, M. J. Schoenberg, V. Verma, A. Csaszar, E. L. Turner, I. Dryanovski, J. Afonso, J. Pascoal, K. N. J. Tsotsos, M. A. Leung, M. Schmidt, O. G. Guleryuz, S. Khamis, V. Tankovich, S. Fanello, S. Izadi, and C. Rhemann. Depth from motion for smartphone ar. *ACM Transactions on Graphics*, 2018.
- [53] A. Vaswani, N. Shazeer, N. Parmar, J. Uszkoreit, L. Jones, A. N. Gomez, L. u. Kaiser, and I. Polosukhin. Attention is all you need. In *NeurIPS*, volume 30, 2017.
- [54] F. Wang, S. Galliani, C. Vogel, and M. Pollefeys. IterMVS: Iterative probability estimation for efficient multi-view stereo, 2022.
- [55] F. Wang, S. Galliani, C. Vogel, P. Speciale, and M. Pollefeys. PatchmatchNet: Learned multi-view patchmatch stereo, 2021.
- [56] K. Wang and S. Shen. MVDepthNet: Real-time multiview depth estimation neural network. In *3DV*, pages 248–257, 2018.
- [57] Y. Wang, W.-L. Chao, D. Garg, B. Hariharan, M. Campbell, and K. Q. Weinberger. Pseudo-lidar from visual depth estimation: Bridging the gap in 3d object detection for autonomous driving. In *CVPR*, June 2019.
- [58] J. Watson, O. M. Aodha, V. Prisacariu, G. Brostow, and M. Firman. The Temporal Opportunist: Self-Supervised Multi-Frame Monocular Depth. In *CVPR*, 2021.
- [59] Z. Xu, Y. Liu, X. Shi, Y. Wang, and Y. Zheng. MARMVS: Matching ambiguity reduced multiple view stereo for efficient large scale scene reconstruction. In *CVPR*, pages 5981–5990, 2020.
- [60] J. Yang, W. Mao, J. M. Alvarez, and M. Liu. Cost volume pyramid based depth inference for multi-view stereo. In *CVPR*, 2020.

- [61] Y. Yao, Z. Luo, S. Li, T. Fang, and L. Quan. MVSNet: Depth inference for unstructured multi-view stereo. *ECCV*, 2018.
- [62] Y. Yao, Z. Luo, S. Li, T. Shen, T. Fang, and L. Quan. Recurrent MVSNet for high-resolution multi-view stereo depth inference. *CVPR*, 2019.
- [63] J. Zbontar and Y. LeCun. Stereo matching by training a convolutional neural network to compare image patches. *Journal of Machine Learning Research*, 17(1-32):2, 2016.
- [64] F. Zhang, V. Prisacariu, R. Yang, and P. H. Torr. GA-Net: Guided aggregation net for end-to-end stereo matching. In *CVPR*, 2019.

In this supplementary material, we show more qualitative results, ablation studies, and the details about network architectures and hyperparameters.

A Network Architectures

Multi-scale Feature Fusion Layer. The fusion layer \mathcal{G} aggregates multi-scale features $f_{i,2} \in \mathbb{R}^{H/2 \times W/2 \times F_0}$, $f_{i,4} \in \mathbb{R}^{H/4 \times W/4 \times F_0}$, $f_{i,8} \in \mathbb{R}^{H/8 \times W/8 \times F_0}$ and $f_{i,16} \in \mathbb{R}^{H/16 \times W/16 \times F_0}$ into a matching feature $f_i \in \mathbb{R}^{H/4 \times W/4 \times F_1}$ at 1/4 scale. Here $F_0=32$ and $F_1=128$ for feature channels, $i = 0$ for the reference image, and $i = 1, \dots, N - 1$ for the source images. The architecture is shown in Fig. 3, including up- and down- sampling, concatenation along the feature channel, a convolution layer Conv0 (with kernel size 3×3 , in- and out- channels 128/128), batch normalization, ReLU, and another convolution layer Conv1 (with kernel size 1×1 , in- and out- channels 128/128).

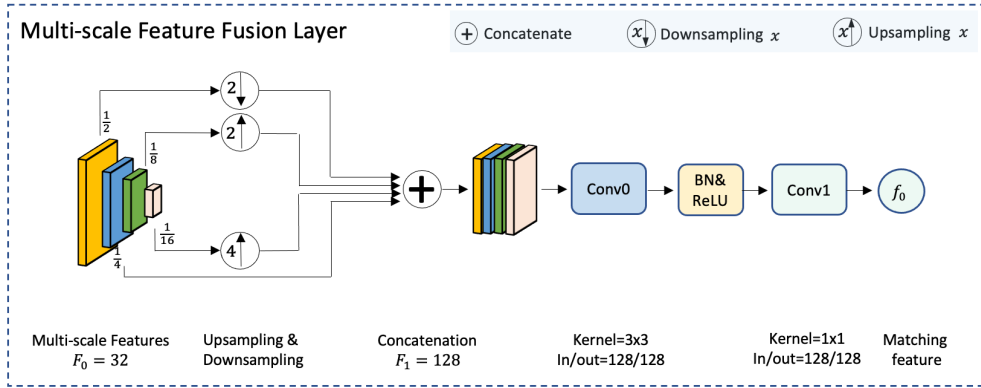


Figure 3: Multi-scale feature fusion layer.

Context Feature Network C-Net. We use the context feature network as in [31, 37, 51], which consists of several residual blocks. It contains around 4.32M parameters.

Model Capacity.

As shown in Tab. 4, the total number of parameters in our network is 27.6M, where residual pose network takes up 47.18%, GRU-based optimizer takes up 25.20%, and the transformer block takes up 1.25%. If not considering the residual pose net, our model then has 14.57M parameters, and most of them are assigned to GRU-based updater, and less capacities are on feature extractors. This kind of capacity configuration makes that our model is not specialized to one domain (for feature extraction), and is well generalized to unseen domains due to the learning to optimize anchored at cost volume via the GRU-based optimizer to predict the index fields for iteratively improved matching.

Network Training and Log Summary. Our network is trained from scratch on the ScanNet training set (with 279,494 samples). It takes around 2 days on 4 NVIDIA RTX A6000 GPUs for up to 20 epochs training. The GRU iteration number is set to 12 for training. The total batch size is 32 (*i.e.*, 8 per GPU). Training image size is 256×256 . We show the log summary of network training

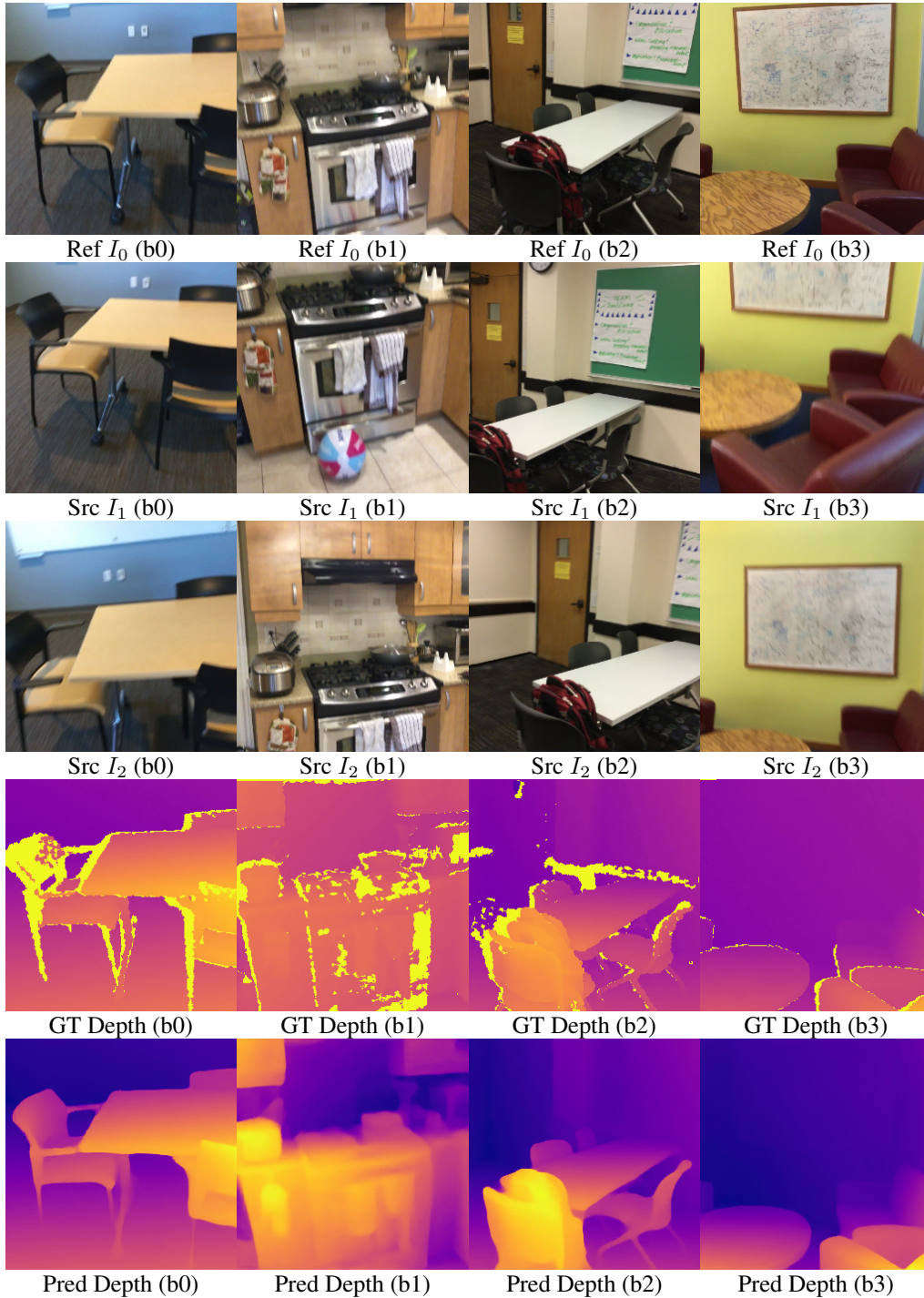


Figure 4: Training logs at last logging step on ScanNet [16] training set. Columns show samples and results of mini-batch ones b0, b1, b2, and b3. For the training logs, we show the color maps of the ground truth depths and predictions in the inverse space (i.e., disparity), so as to better align with the training loss calculated on the inverse depth domain.

Layers	F-Net	C-Net	Transformer	Residual Pose Net	GRUs	Total
Parameter (M)	2.9545	4.3212	0.3438	13.0120	6.9501	27.5816
Percentage	10.70%	15.67%	1.25%	47.18%	25.20%	100%

(a) Our model capacity (full version).

Layers	F-Net	C-Net	Transformer	Residual Pose Net	GRUs	Total
Parameter (M)	2.9545	4.3212	0.3438	-	6.9501	14.5696
Percentage	20.28%	29.66%	2.36%	-	47.70%	100%

(b) Our model capacity, if without residual pose net.

Table 4: Our model capacity. Parameter numbers are given in million (M) and the percentage of each module is listed.

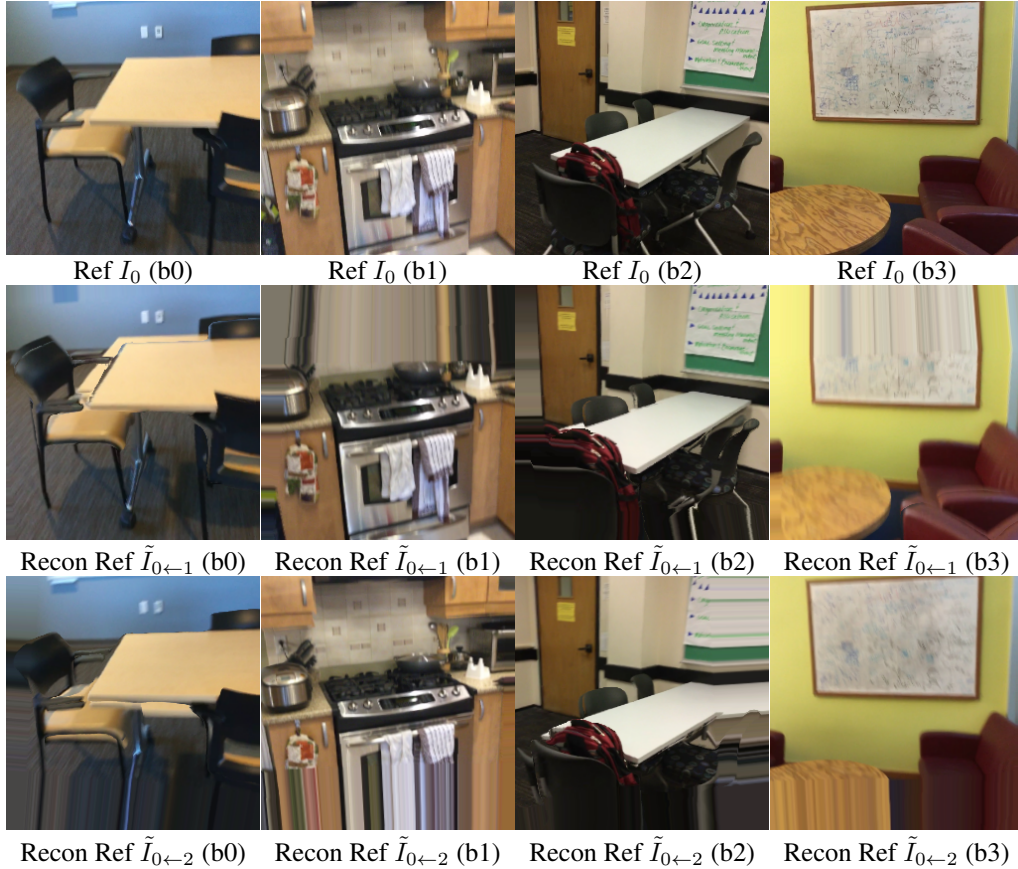


Figure 5: Residual pose training. The top row shows the reference images, and the bottom two rows show the reconstructed images of the reference view by warping the source images with the updated poses and predicted depth map of the reference view.

at the last logging step (i.e., step=99,609). From the top to bottom, Fig. 4 shows a batch of input samples (batch size = 4 for logging), including reference images I_0 and two source images I_1 and I_2 , the ground truth depth maps and our depth predictions. The residual pose net is supervised by the photometric loss as shown in Fig. 5. We do one epoch warmup training only for the residual pose net with other layers frozen.

GRU Iterative Updates. Fig. 6 illustrates the iterative estimation of depth maps. For better visualization, we put the reference images and the ground truth depths on the first two rows. The bottom 4 rows show the depth predictions at iteration step $t = 0, 4, 8, 12$ for each batch sample. *Itr-0* means the softargmin-start we introduced to accelerate the GRU training and convergence. We can

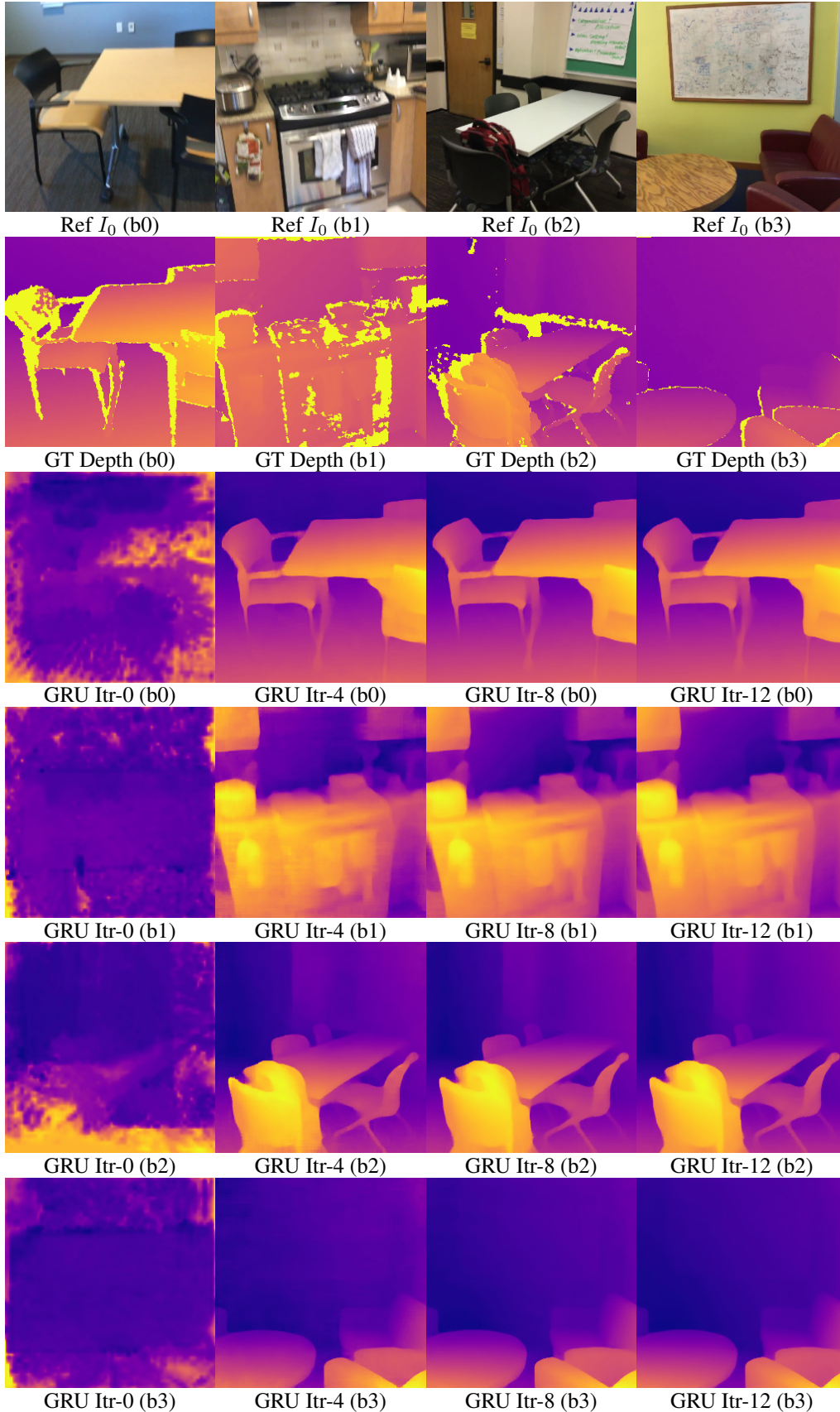


Figure 6: Iterative depth estimation from GRU layers. The bottom 4 rows show the depth predictions at iteration step $t = 0, 4, 8, 12$ for each batch sample.

see the depth maps are progressively improved within T iterations (here $T = 12$ in network training for the trade-off between the memory consumption and depth accuracy).

Network Inference. For inference, we set the GRU iteration number as $T = 24$ by default, and we also ablate other values of T in the main paper. The input image is in 320×256 resolution, and it is upsampled to 640×320 for ScanNet benchmark evaluation and cross-dataset generalization. The GPU memory consumption is 2088MiB from nvidia-smi, and runtime in inference mode is 8.6 fps, when processing frames with dimension 320×256 .

B Ablation Studies

We introduce more ablation studies to verify our design.

Global Matching Feature of Reference View. The asymmetric employment of the transformer block to the reference frame, provides accurate matching features for cost volume construction. We compare our transformer layer with another way similar to the GMA module in [31], which applies the transformer layer to motion feature for improved optical flow estimation based on [51]. We applied the same transformer layer to the GRUs layers, but found worse results when evaluated on the ScanNet test set, with *abs* error increased from 0.1392 meters to 0.1621 meters.

Different Depth Binning. When implementing plane-sweep stereo [15, 20] to construct the cost volume, we need to sample $M_0=64$ plane hypotheses. In our main experiments, we use the inverse depth bins, *i.e.*, the plane hypotheses is uniformly sampled in the inverse depth space, *s.t.* $1/d \sim U(d_{\min}, d_{\max})$. Here we set $d_{\min}=0.25$ and $d_{\max}=20$ meters for indoor scenes (e.g., ScanNet [16]). We also test linear depth bins, *i.e.*, $d \sim U(d_{\min}, d_{\max})$, and hand-crafted depth bins by calculating the depth distribution on ScanNet. But we found the inverse depth binning achieves the best results, as we reported in the main paper. We also test adaptive depth bins as in [5], where the depth bins are dynamically generated conditioned on the global feature learned by a transformer layer. For our(+pose) variant, adaptive depth bins lead to marginal improvement than the inverse depth bins. However, for our(+pose,atten) variant, adaptive depth bins hinder the depth accuracy.

C Qualitative Results

Depth and Error Maps. We presents more qualitative results of depth maps and error maps on the ScanNet test set [16] in Fig. 7. The samples shown here are scene0711_00/001050.png, scene0711_00/002530.png, scene0727_00/001260.png, and scene0769_00/000720.png. The error maps contain the absolute errors *abs* in depth. For the ground truth depth maps and the error maps, invalid regions (*i.e.*, without ground truth depth annotation) are filled in black. The color maps of the ground truth depths and predictions are shown in the depth space (*i.e.*, not in disparity space). The *abs* errors (in meter) are superimposed on the error maps for better comparison. The corresponding color bar to visualize the error maps is shown in Fig. 8. Comparing the depth predictions and the error maps for our method and the baseline IterMVS [54] and baseline PairNet [18], our method predicts more accurate estimates, especially in the challenging regions, *e.g.*, the boundary, the ground, the white wall, and the round desk.

D Quantitative Metrics

We use the metrics defined in [19], including mean absolute error (*abs*), mean absolute relative error (*abs-rel*), squared relative error (*sq-rel*), RMSE in linear (*rmse*) and log (*rmse-log*) scales, and inlier ratios under thresholds of $1.25/1.25^2/1.25^3$. For a predicted depth map y and ground truth y^* , each with n pixels indexed by i , those metrics are formulated as:

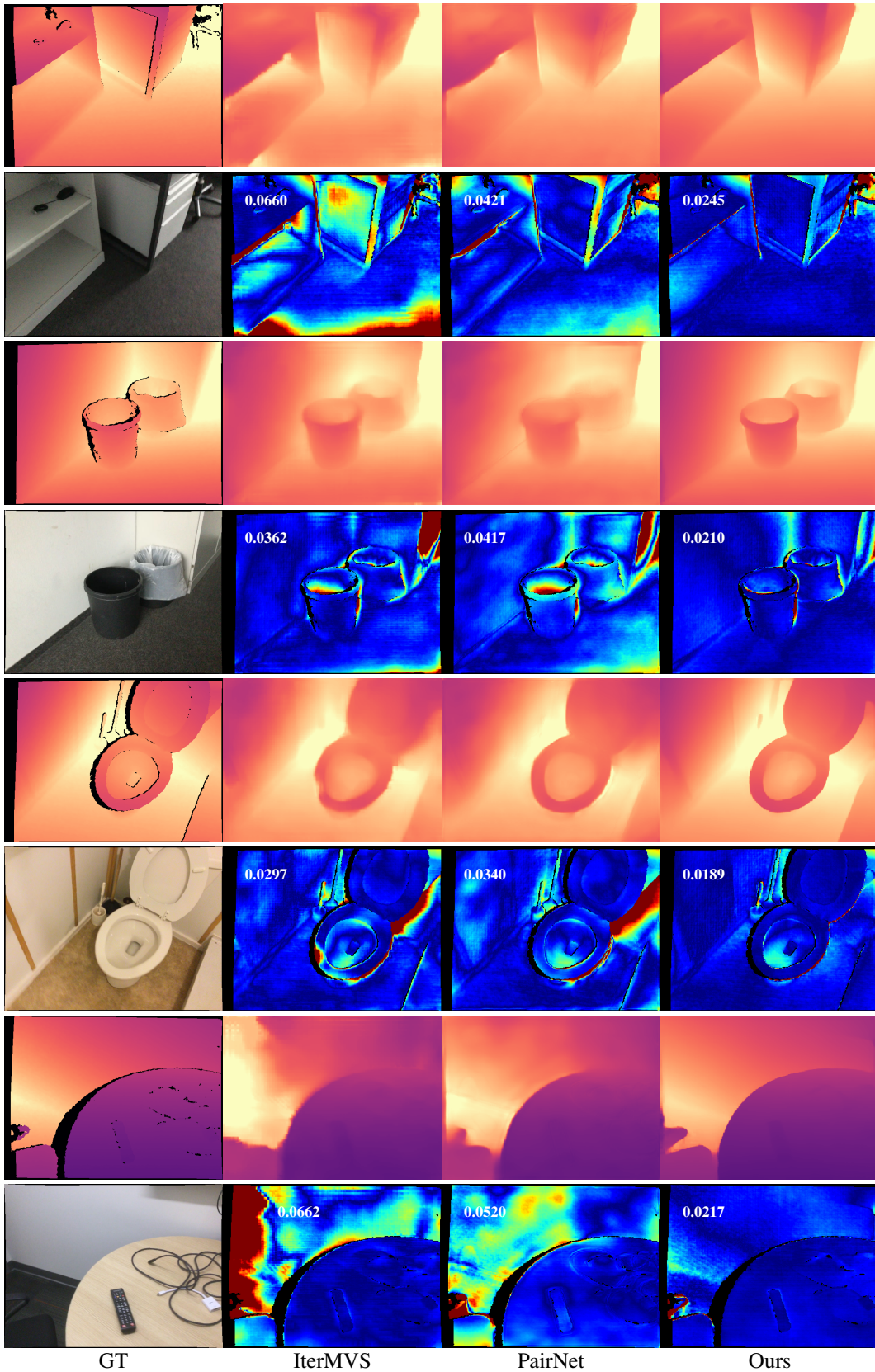


Figure 7: Qualitative results on ScanNet [16] test set. Every two rows show depth maps (top) and error maps (bottom) for a sample. The leftmost column shows ground truth depths and reference images. Others are the depth predictions and error maps, by IterMVS [54], PairNet [18] and ours, respectively.

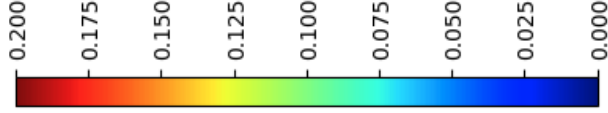


Figure 8: Color scale used for all *abs* error in depth maps in the supplementary material.

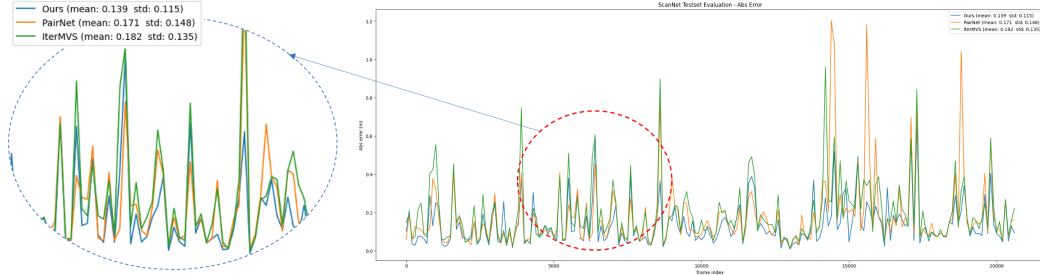


Figure 9: Absolute error metric curves evaluated on all the frames of ScanNet [16] test set, for our method and baselines IterMVS [54] and PairNet [18]. Please zoom in the figures for the metrics and legends shown in top left.

$$\text{abs} : \frac{1}{n} \sum_i |y_i - y_i^*|$$

$$\text{abs-rel} : \frac{1}{n} \sum_i |y_i - y_i^*|/y_i^* \quad \text{sq-rel} : \frac{1}{n} \sum_i \|y_i - y_i^*\|^2/y_i^*$$

$$\text{rmse} : \sqrt{\frac{1}{n} \sum_i \|y_i - y_i^*\|^2}$$

$$\text{rmse-log} : \sqrt{\frac{1}{n} \sum_i \|\log y_i - \log y_i^*\|^2}$$

$$\text{inlier ratio\% of } y_i \quad \text{s.t.} \quad \max\left(\frac{y_i}{y_i^*}, \frac{y_i^*}{y_i}\right) = \delta < 1.25/1.25^2/1.25^3$$

The ScanNet test set in our experiments contains 20,668 samples. As shown in Fig. 9, we report *abs* error curves (by plotting values in meter every 100 frames, out of those 20,668 samples) to reflect the distribution of the errors. We also compare the mean and standard deviation to reflect the overall performance of our method versus the baselines: mean error 0.139 (our) < 0.171 (PairNet) < 0.182 (IterMVS), and standard deviation 0.115 (our) < 0.135 (IterMVS) < 0.148 (PairNet), showing that our method consistently outperforms the baselines with smaller average and lower standard deviation.